ACS APPLIED MATERIALS & INTERFACES

www.acsami.org

Research Article

Self-Assembly of Antifouling Wavy Taco Shell Arrays Inspired by Hierarchically Wrinkled Shark Scales

Hsiang-Wen Hsueh, Shin-Hua Lin, Zi-Xuan Chen, Hsin-Yi Yang, Yun-Yu Wu, Han-Yu Hsueh, Rong-Ho Lee, Hsiu-Wen Chien,* and Hongta Yang*

Cite This: *ACS Appl. Mater. Interfaces* 2026, 18, 30329−30339

Read Online

ACCESS | Metrics & More | Article Recommendations | Supporting Information

ABSTRACT: Shortfin mako sharks are armored with riblet-like scales, measuring tens to hundreds of micrometers and oriented toward their caudal fins. These well-organized features are known to reduce hydrodynamic drag by regulating boundary layer flow, thereby enabling rapid locomotion and facilitating the removal of attached microorganisms in marine environments. Interestingly, the scales located in the caudal peduncle are superimposed with oriented microwrinkles that promote antifouling performance under low-velocity flow regimes, which guide the design of the antifouling coatings. Bioinspired by shark scales, a self-assembly methodology is developed to engineer hierarchical wrinkle arrays with tunable structural geometries. These architectures induce pronounced anisotropic antiwetting behavior and provide weak microbial anchoring sites, thereby enhancing the efficiency of microbial removal. The influence of structural geometries on the antifouling performance has also been systematically evaluated in this research. It is anticipated that such hierarchically wrinkled structures will provide an environmentally sustainable strategy for manufacturing advanced antifouling coatings applicable to biomedical, marine, and fluid transport applications.

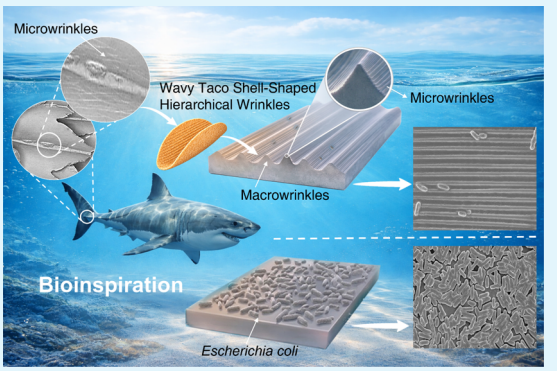

KEYWORDS: *shark scales, antifouling, bioinspiration, self-assembly, hierarchical wrinkle arrays*

INTRODUCTION

Biofouling, characterized by the accumulation of bacteria, fungi, algae, or other undesirable microorganisms on surfaces, poses considerable challenges across a wide range of applications.[1−3] In particular, it adversely affects industrial facilities, medical devices, underwater instruments, and daily use items by reducing operational efficiency, accelerating material degradation and structural deterioration, and increasing maintenance requirements and associated costs. To mitigate these issues, a broad spectrum of antifouling strategies has been implemented, including the utilization of biodispersants or biocides, ultrasonic cleaning, thermal treatments, and ultraviolet or pulsed-laser irradiation, which aim to eradicate microorganisms or inhibit their settlement on surfaces.[4−8] Nevertheless, conventional chemical antifouling agents, exemplified by ethoxylated alcohols, sulfosuccinates, sorbitan esters, sodium hypochlorite, and tributyltin, inevitably cause severe toxicity to marine living creatures.[9−12] Rather than inducing direct microbial death, energy input can inactivate or denature microorganisms in aqueous systems. Unfortunately, such methodologies require high power consumption, and the resulting thermal discharge may lead to unintended environmental impacts.

Over the past decade, a variety of fluoropolymers have been developed for use as environmentally benign antifouling coatings.[13−15] Owing to their inherently low surface energies, these coatings effectively suppress microbial adhesion and proliferation and facilitate biofouling removal. However, most of the fluoropolymers are constrained by insufficient mechanical strength and limited environmental resistance. In recent years, zwitterionic polymers, which possess equal numbers of anionic and cationic groups within the same monomer unit, have emerged as promising candidates for the design of advanced antifouling coatings.[16−18] The introduction of zwitterions allows the polymers to strongly bind water molecules through electrostatic interactions, thereby forming a stable hydration layer that resists microbial adhesion and biofouling. Nevertheless, the large-scale fabrication of zwitterionic polymers remains technically challenging, which restricts their practical and commercial applications. Therefore, there is an urgent demand to design and develop antifouling coatings.

Across approximately 3.8 billion years of natural selection, living organisms have evolved a remarkable diversity of

Received: March 30, 2026
Revised: May 10, 2026
Accepted: May 11, 2026
Published: May 20, 2026

https://doi.org/10.1021/acsami.6c06369
ACS Appl. Mater. Interfaces 2026, 18, 30329−30339

structural architectures that enable adaptation to harsh environmental conditions. For instance, low surface energy waxy nano- and microstructures present on the surfaces of Formosan subterranean termite (*Coptotermes formosanus* Shiraki) wings, bear cicada (*Cryptotympana takasagona* Kato) wings, nasturtium (*Tropaeolum*) petals, prickly pear (*Opuntia*) skins, and lotus (*Nelumbo nucifera*) leaves allow air to be trapped within the hierarchical structures, resulting in enhanced surface hydrophobicity and enhanced self-cleaning functionality.[19−23] Despite their superhydrophobic characteristics, the water-repellent architectures are insufficient to suppress biofilm and slime layer formation. The enlarged surface roughness inherently facilitates microbial colonization. Compared with these natural prototypes, cartilaginous fish skins are armored with densely packed placoid scales.[24,25] These riblet-like scales not only provide protection against predators but also significantly reduce overall hydrodynamic drag forces, thereby promoting efficient aquatic locomotion and limiting the attachment of algae and microbes. It is worth noting that the scales exhibit pronounced morphological heterogeneities across distinct body regions, indicative of their specialized adaptation to localized hydrodynamic environments. Taking the caudal region as an example, the fluid experiences a discernible reduction in velocity, which contributes to the generation of propulsive forces. Undoubtedly, the resulting low-shear flow environment is prone to biofouling, necessitating the development of more effective antifouling mechanisms. To boost the antifouling capability, the riblet-like scales situated within the caudal peduncle are covered with oriented micrometer-scale wrinkles, establishing weak anchoring sites for microorganisms.[26] It is of vital importance that such a structural configuration can further enhance momentum transfer and shear stress to release biofouling.[27]

Drawing inspiration from the distinctive surface topologies, a variety of shark scale-patterned coatings have been realized using soft lithography.[28−30] Unfortunately, those antifouling structures, templated from natural biomaterials, exhibit inconsistent structural morphologies and nonuniform structural arrangements. Leveraging rapid advancements in top-down microfabrication technologies, precisely organized wrinkles with sizes ranging from tens to hundreds of micrometers have been engineered for antifouling applications in the past few years.[31−33] However, most photolithography-based methodologies remain constrained by high fabrication costs, limited production throughput, and the need for costly commercial masks. Alternatively, bottom-up self-assembly methodologies provide a facile, scalable, and cost-effective strategy to construct symmetric wrinkle arrays.[34−36] As exemplified by interfacially release-controlled approaches, wrinkled structures are generated through the release of localized strain in multilayer composite systems, driven by disparities in elastic moduli between adjacent layers. The self-assembled architectures can subsequently be utilized as elastomeric stamps, enabling on-demand patterning of large-area wrinkle arrays on miscellaneous substrates. Although the as-fabricated wrinkle arrays demonstrate anisotropic antiwetting characteristics and support directional liquid transport, their antifouling performances are not substantially enhanced either under hydrodynamic conditions or in water-deficient environments.[37−39] Moreover, hierarchical structures composed of macrowrinkle arrays overlaid with microwrinkle features, which are anticipated to play a pivotal role in determining the antifouling performance, have seldom been achieved.[40]

In this study, a multistage surface treatment methodology is developed to enable the assembly of hierarchical wrinkle arrays with precisely tunable structural geometries. The presence of microwrinkles greatly diminishes the interfacial interactions with water and creates weak anchoring sites for microorganisms. As a consequence, the structured surfaces exhibit pronounced anisotropic antiwetting characteristics and low microbial adhesion, thereby facilitating efficient removal of microorganisms upon rinsing with water along the direction parallel to the hierarchical wrinkles. The enhanced antifouling capability, derived from nontoxic and eco-friendly mechanisms inspired by shark scales, highlights its considerable potential for practical applications.

EXPERIMENTAL SECTION

Materials and Chemical Reagents

A shortfin mako shark (*Isurus oxyrinchus*) specimen, with an overall length of 1.31 m, was collected from the Pacific Ocean in the vicinity of Taiwan. Glutaraldehyde (∼25.0% aqueous solution) and anhydrous ethanol (≥99.5%, 200 proof), employed to pretreat the shark skins, were supplied by Merck KGaA. Deionized water (18.4 MΩ·cm), purified by a Milli-Q EQ 7016 water purification system, was used directly in all experiments. Sylgard 184 poly(dimethylsiloxane) (PDMS) precursor kits, consisting of a thermal-curable base and a curing agent, were procured from Dow Corning. Photocurable SR 454 ethoxylated trimethylolpropane triacrylate (ETPTA) oligomers (≥99.5%) and the corresponding photoinitiator, Darocur 1173 2-hydroxy-2-methyl-1-phenyl-1-propanone (HMPP, ≥97.0%), were acquired from Sartomer Americas and BASF SE, respectively. 1*H*,1*H*,2*H*,2*H*-Heptadecafluorodecyl acrylate (HDFDA, ≥97.0%), utilized as a surface modifier, was provided by Merck KGaA. ATCC 21351 *Staphylococcus aureus* (*S. aureus*) and ATCC 23501 *Escherichia coli* (*E. coli*), the model bacterial strains used in this study, were sourced from the Food Industry Research and Development Institute in Taiwan. Tryptic soy broth, employed as a culture medium, was obtained from Cyrusbioscience. Sterile-filtered phosphate-buffered saline (pH 7.4, 0.8%), utilized as a sterile saline solution, was supplied by Gold Biotechnology. A lactate dehydrogenase assay kit, containing Triton X-100 (≥97.0%), sodium L-lactate (≥99.0%), sucrose (≥99.0%), β-nicotinamide adenine dinucleotide hydrate (≥96.5%), diaphorase (≥95.0%), 2-(4-iodophenyl)-3-(4-nitrophenyl)-5-phenyltetrazolium chloride (≥98.0%), bovine serum albumin (≥98.0%), and sodium oxamate (≥99.7%), was purchased from Thermo Fisher Scientific. All chemical reagents were utilized as received.

Fabrication of Shark Scale-Patterned Substrates

Fresh shark skins were collected from the caudal peduncle and lateral region of a shortfin mako shark. After removing dermal and subcutaneous tissues with a razor blade, the skin specimens were rinsed with deionized water to eradicate any residual biological matter. The cleansed skin specimens were sandwiched between two microscope slides and then immersed in an aqueous glutaraldehyde solution (3.0%) for 5.5 h to maintain their structural integrity. Subsequently, these specimens were dehydrated through a series of ethanol washes at progressively increasing ethanol concentrations (25.0, 50.0, 75.0, and 99.5%), followed by air-drying under ambient conditions. Afterward, a degassed PDMS base/curing agent mixture, in a 10:1 weight ratio, was poured over these shark skins. Once the mixture was fully cured at 60 °C, the skins could be easily peeled away to generate PDMS negative replicas. A photocurable ETPTA oligomer/HMPP mixture, in a 50:1 volume ratio, was then cast onto the as-fabricated PDMS replicas and photopolymerized by exposure to UV irradiation in an OPAS XLite 500Q curing system. Owing to the high elasticity and low surface energy of PDMS, the

https://doi.org/10.1021/acsami.6c06369
ACS Appl. Mater. Interfaces 2026, 18, 30329−30339

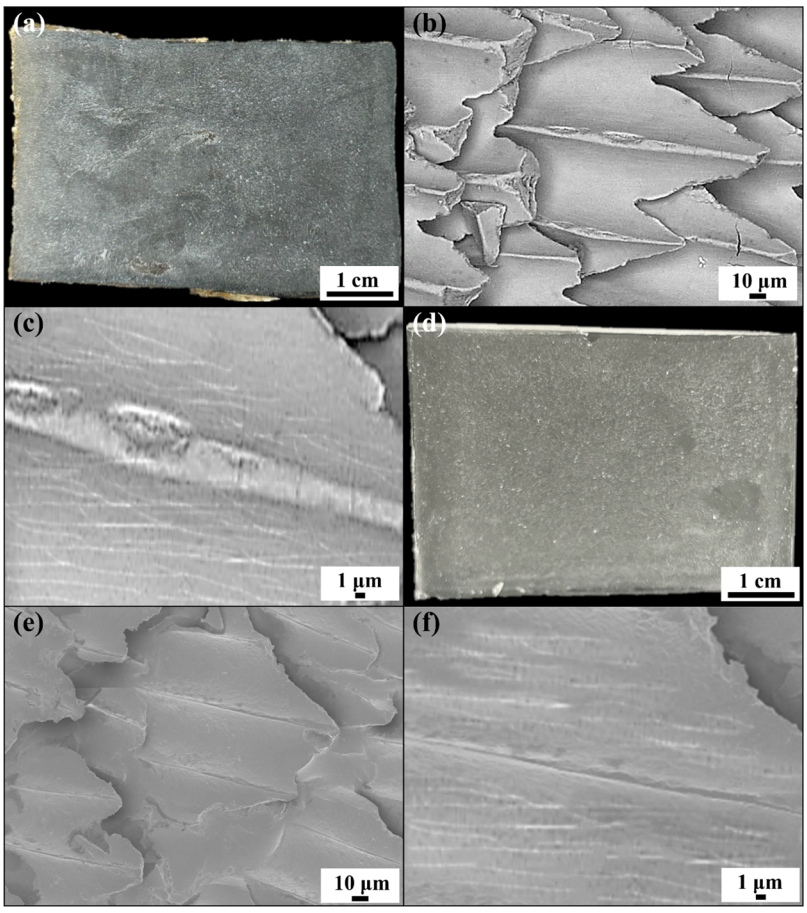

Figure 1. (a) Photographic image, (b) top-view SEM image, and (c) magnified top-view SEM image of the skin surface located within the caudal peduncle of a shortfin mako shark. (d) Photographic image, (e) top-view SEM image, and (f) magnified top-view SEM image of a shark scale-patterned poly(ETPTA) substrate templated from this shark skin.

shark scale-patterned poly(ETPTA) substrates could be demolded without inducing significant deformation.

Self-Assembly of Oriented Microwrinkle Patterns and Macrowrinkle Patterns

A degassed mixture of PDMS base/curing agent, in a 30:1 weight ratio, was molded into cuboids with dimensions of 10.0 × 10.0 × 0.5 cm (length × width × height) and then cured at 60 °C. The cuboidal PDMS film could be elongated uniaxially at a fixed stretching rate of 5.0 cm/min using a GOTECH A1-7000-ST electromechanical universal testing machine. As an elongation ratio of 40% was achieved, the surface of this stretched film was modified by exposure to oxygen plasma for 2.5 min in a JunSun Tech UDS reactive ion etcher, operating at a fixed chamber pressure of 20 mTorr and a power density of 20 W/cm^2. On account of the elastic modulus mismatch between the oxygen plasma-treated surface and the underlying elastic substrate, oriented microwrinkles with an average wavelength of 1 μm were spontaneously generated once this stretched film was relaxed. Afterward, the resulting PDMS film was employed as a replica mold to pattern the microwrinkle array onto a poly(ETPTA) substrate through the aforementioned soft lithographic approach. In addition to the microwrinkle patterns, well-arranged macrowrinkle patterns featuring specific structural geometries could be designed and built. In the fabrication process to create classic chip-shaped macrowrinkles, featureless PDMS films were subjected to uniaxial stretching until their elongation ratios reached 25%. Subsequently, these stretched films were exposed to UV irradiation/ozone for varied durations, respectively, in a Qing QUT-400 drawer-type UV curing chamber. Upon releasing the applied strains, oriented macrowrinkles with wavelengths and amplitudes on demand were formed on the UV/ozone-treated surfaces, attributed to the different disparities in elastic moduli between the stiffened surface layers and the underlying substrates. These PDMS replica molds were further utilized to pattern chip-shaped macrowrinkle arrays onto poly(ETPTA) substrates. Instead of an elongation ratio of 25%, featureless PDMS films could be uniaxially elongated to a strain of 50%. Following this, the previously described fabrication process was applied to pattern-oriented crunchy taco shell-shaped macrowrinkles with tunable wavelengths and amplitudes onto poly(ETPTA) substrates.

Self-Assembly of Shark Scale-Inspired Hierarchical Wrinkle Arrays

The hierarchical wrinkle arrays were self-assembled through a multistage surface treatment process. In the initial stage, a bare PDMS film was uniaxially stretched to an elongation ratio of 65% and subsequently exposed to oxygen plasma for 2.5 min. The stretched film was then gradually relaxed to an elongation ratio of 25%, during which a microwrinkle array spontaneously formed on the oxygen-plasma-treated stiff surface. For the second stage, the wrinkled PDMS film was further subjected to prolonged UV irradiation/ozone treatment to induce the emergence of a stiff layer, which was substantially thicker than that generated during the initial plasma exposure. The complete release of the remaining strain subsequently produced a microwrinkle-patterned macrowrinkle array. Afterward, the resulting PDMS film served as a replica mold for patterning a wavy chip-shaped hierarchical wrinkle array via a soft lithographic strategy. Notably, wavy taco-shell-shaped hierarchical wrinkles could also be developed. To prepare the replica mold on-demand, a featureless PDMS film was uniaxially stretched to an elongation ratio of 90%. After undergoing a 2.5 min oxygen plasma treatment, the stretched film was partially relaxed to an elongation ratio of 50%. Subsequently, this PDMS film was exposed to UV irradiation/ozone,

https://doi.org/10.1021/acsami.6c06369
ACS Appl. Mater. Interfaces 2026, 18, 30329−30339

after which the remaining strain was fully released. As a result, a macrowrinkle array superimposed with microwrinkle features was developed on the surface. This PDMS film was further employed to pattern a wavy taco-shell-shaped hierarchical wrinkle array.

Surface Functionalization of the Wrinkle Arrays

To reduce surface energies of the wrinkle arrays, the wrinkle-patterned poly(ETPTA) substrates were surface-functionalized with fluorides via chemical vapor deposition. During the chemical functionalization process, the poly(ETPTA) substrates were transferred into a vacuum oven preloaded with a vial containing liquid 1*H*,1*H*,2*H*,2*H*-heptadecafluorodecyl acrylate (HDFDA), a fluorinated acrylate compound comprising 17 fluorine atoms. Upon reaching 85 °C, the HDFDA could be vaporized below its intrinsic boiling point under vacuum conditions and then reacted with the acrylate groups of poly(ETPTA).[41] After 1 h, these fluoride-functionalized poly(ETPTA) substrates were transferred into a vacuum chamber to ensure the complete removal of unreacted HDFDA molecules.

Characterization of Surface Morphologies

A Sony DSC-RX10 IV digital camera was employed to capture the photographic images of the specimens. The corresponding surface topographical features were characterized using a Leica DM4 optical microscope, complemented by a Keyence VK-X1000 3D laser scanning confocal microscope (LSCM) and a JEOL JSM-IT810 field-emission scanning electron microscope (FE-SEM). Before SEM imaging, the specimens were sputter-coated with a gold layer by using a Ted Pella 208HRD vacuum coating system.

Water Contact Angle Measurements

Antiwetting behaviors, including static water contact angles, advancing water contact angles, receding water contact angles, and sliding angles of water drops, were characterized by a Krüss DSA 10 MK2 drop shape analysis system equipped with Hamilton autopipetting and imaging systems. Deionized water, collected from a Milli-Q EQ 7016 water purification system, was used directly for all the measurements. Before the measurements, the surface-functionalized wrinkle-patterned poly(ETPTA) substrates were cleaned by applying filtered air to remove surface contaminants. Water drops with a fixed volume of 7.5 μL were then dispensed onto the cleansed substrates using the automated pipetting system, after which their images were captured. Afterward, the static and dynamic water contact angles were determined from the images using ImageJ v1.37c with the DropSnake and LBADSA plugins. For each poly(ETPTA) substrate, measurements were performed at five distinct regions, and the average values were reported.

Evaluation of Antifouling Performances

The antifouling properties were characterized by assessing bacterial adhesion on the surface-functionalized wrinkle-patterned poly(ETPTA) substrates. *S. aureus* and *E. coli* were cultured aerobically in tryptic soy broth at 37 °C for 24 h and then were dispersed in phosphate-buffered saline at neutral pH. The concentration of each bacterial suspension was controlled to be ~1 × 10^9 CFU/mL. Afterward, 1 mL of the bacterial suspension was deposited onto each poly(ETPTA) substrate (1 cm^2 in size), followed by incubation at 37 °C with shaking at 100 rpm for 12 h. Subsequently, these poly(ETPTA) substrates were rinsed with phosphate-buffered saline to eliminate nonadhering bacteria, and the bacteria that adhered were lysed by immersing the substrates in a Triton X-100/phosphate-buffered saline solution (0.5%) at 37 °C for 30 min. After that, 100 μL of each bacterial lysate was mixed with an equivalent volume of a working solution, composed of phosphate-buffered saline, sodium L-lactate (54.0 mg/mL), sucrose (48.0 mg/mL), β-nicotinamide adenine dinucleotide (12.0 mg/mL), diaphorase (5.4 mg/mL), 2-(4-iodophenyl)-3-(4-nitrophenyl)-5-phenyltetrazolium chloride (2.0 mg/mL), and bovine serum albumin (1.2 mg/mL). These resulting mixtures were incubated at 37 °C for 1 h to initiate the lactate dehydrogenase-mediated colorimetric reaction, which could then be terminated by introducing 50 μL of a sodium oxamate/phosphate-buffered saline solution (16.0 mg/mL). The lactate dehydrogenase present in the mixture was quantified spectrophotometrically at 490 nm using a BMG LABTECH SPECTROstar Nano microplate reader to determine the number of bacteria remaining on each poly(ETPTA) substrate.

RESULTS AND DISCUSSION

Shortfin mako shark skins are covered with densely packed dermal denticles, commonly referred to as placoid scales. The

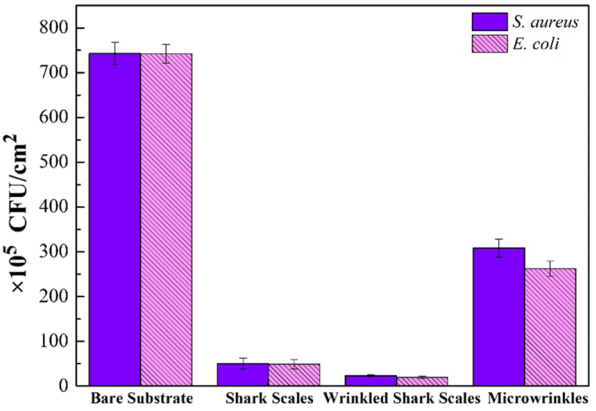

Figure 2. Quantitative analysis of the bacterial colony-forming units (CFU/cm^2) on a surface-functionalized featureless poly(ETPTA) substrate, a surface-functionalized shark scale-patterned poly(ETPTA) substrate, a surface-functionalized wrinkled shark scale-patterned poly(ETPTA) substrate, and a surface-functionalized microwrinkle-patterned poly(ETPTA) substrate. The solid and slashed columns represent the bacterial colony-forming units of *S. aureus* and *E. coli*, respectively.

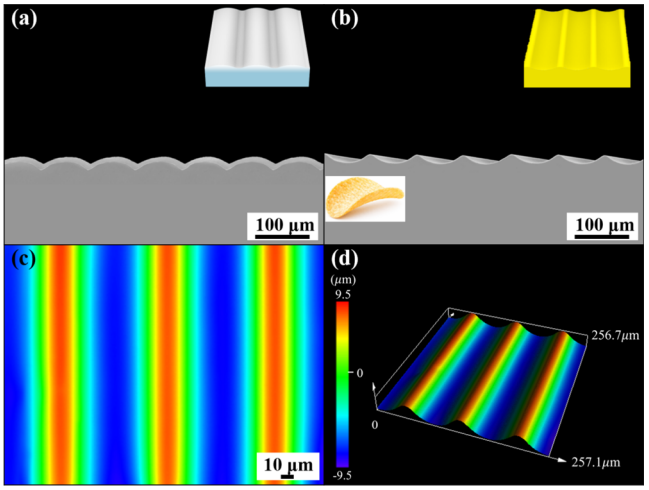

Figure 3. (a) Cross-sectional SEM image of a PDMS mold fabricated by uniaxially stretching a featureless PDMS film to an elongation ratio of 25%, followed by a UV irradiation/ozone treatment for 50 min. (b) Cross-sectional SEM image of a classic chip-shaped macrowrinkle array-patterned poly(ETPTA) substrate replicated from the PDMS mold. (c) Top-view and (d) tilted-view LSCM images of the classic chip-shaped macrowrinkle array-patterned poly(ETPTA) substrate.

placoid scales exhibit riblet-like structural features, with ridge heights and inter-ridge spacings on the scale of several tens of micrometers.[24] It is worth mentioning that these structural features are directed toward the shark's caudal fin, facilitating the guidance of seawater flow and hence suppressing microbial attachment. Interestingly, the placoid scales even possess distinct surface morphologies across different body regions.

https://doi.org/10.1021/acsami.6c06369
ACS Appl. Mater. Interfaces 2026, 18, 30329−30339

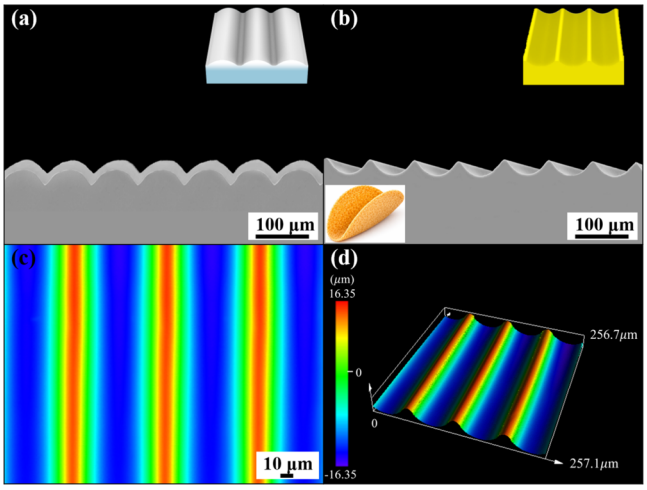

Figure 4. (a) Cross-sectional SEM image of a PDMS mold fabricated by uniaxially stretching a featureless PDMS film to an elongation ratio of 50%, followed by a UV irradiation/ozone treatment for 50 min. (b) Cross-sectional SEM image of a crunchy taco shell-shaped macrowrinkle array-patterned poly(ETPTA) substrate replicated from the PDMS mold. (c) Top-view and (d) tilted-view LSCM images of the crunchy taco shell-shaped macrowrinkle array-patterned poly(ETPTA) substrate.

Compared with the scales found on the lateral skin surface (Figure S1), it is apparent that the ones situated in the caudal peduncle are superimposed with oriented microwrinkles (Figure 1). The presence of microwrinkles not only diminishes microbial anchoring strength but also enhances unidirectional fluid transfer, thereby enabling more effective removal of biofouling within the caudal peduncle region.[26]

To corroborate this finding, these shark skin specimens are used as structural templates to replicate riblet-like and microwrinkle-covered riblet-like hierarchical features onto poly(ETPTA) substrates through a conventional soft lithographic strategy (Figure S2). The shark scale-patterned poly(ETPTA) substrates are subsequently surface-functionalized with 1*H*,1*H*,2*H*,2*H*-heptadecafluorodecyl acrylate (HDFDA) to lower their surface energies. As shown in Figure S3, surface functionalization with fluorinated groups significantly increases the static water contact angle and reduces the corresponding water contact angle hysteresis, thereby enhancing the water repellency of poly(ETPTA). Undoubtedly, the introduction of riblet-like structural features effectively reduces water droplet−surface interactions, thus inducing significant enhancements in surface hydrophobicity. In comparison with the static and dynamic water contact angles found on a surface-functionalized featureless poly(ETPTA) substrate, it is evident that the angles are substantially increased on these surface-functionalized shark scale-patterned poly(ETPTA) substrates (Figures S4 and S5). The elevation of dynamic water contact angles further leads to a concomitant reduction in water contact angle hysteresis and sliding angles. It is noteworthy that the sliding angles acquired in the direction perpendicular to the templated riblet-like structural features are consistently smaller than those measured parallel to the features. Crucially, a more pronounced difference in sliding angle is observed for the microwrinkle-covered riblet-like hierarchical features. The results demonstrate enhanced anisotropic antiwetting behavior on hierarchically wrinkled structures. This unique characteristic allows water in contact with the surface to transport preferentially in the direction parallel to the structural features, thereby facilitating the removal of microbes upon rinsing the surface with aqueous solutions along this direction. Accordingly, the hierarchically wrinkled structures exhibit minimal bacterial colony-forming units of both spherical *S. aureus* and rod-like *E. coli* (Figure 2 and Figure S6). In contrast, a surface featuring solely a microwrinkled structure array, with an average wavelength and amplitude of approximately 1 μm, shows a limited reduction in water-surface contact area, and consequently displays only modest enhancement in surface hydrophobicity and weak anisotropic antiwetting behaviors (Figures S7 and S8). As a result, inefficient bacterial removal is observed on the surface-functionalized microwrinkle-patterned poly(ETPTA) substrate.

Drawing inspiration from the scales of shortfin mako sharks, well-organized macrowrinkle arrays with tunable structural geometries are designed and built to realize anisotropic antiwetting and antifouling functionalities. In the fabrication procedures, PDMS macrowrinkles with precisely controlled wavelengths, amplitudes, and orientations are self-assembled upon releasing uniaxially stretched PDMS substrates (strain = 25%) that have been subjected to UV/ozone treatment for varying durations (Figure S9). It is found that prolonged UV/ozone treatment amplifies the elastic modulus mismatch between the stiffened surface layer and the underlying substrate, thereby inducing the formation of macrowrinkles with larger wavelengths and amplitudes (Figure 3 and Figures S10−S12).[42] The PDMS macrowrinkles aligned perpendicular to the elongation direction are then employed as stamps to pattern classic chip-shaped macrowrinkle arrays onto poly(ETPTA) substrates. It is worth mentioning that both the wavelength and amplitude of classic chip-shaped macrowrinkles increase monotonically with increasing UV/ozone treatment duration. Specifically, extending the treatment period from 30, 40, 50 to 60 min increases the macrowrinkle wavelength from 50.2, 69.8, 90.9 to 110.3 μm, accompanied by an increase in amplitude from 5.2, 7.5, 9.8 to 11.9 μm (Figure S13), respectively. The approximately linear dependence of both wavelength and amplitude on treatment period within the examined range offers a straightforward approach for tailoring macrowrinkle dimensions. However, the introduction of classic chip-shaped macrowrinkles does not substantially reduce the projected solid area fraction and hence yields an average static water contact angle of approximately 121.3° (Figures S14 and S15). Among these macrowrinkle arrays, the one replicated from a PDMS stamp subjected to 50 min of UV/ozone treatment shows a slightly higher static water contact angle, measuring 124 ± 2°. The antiwetting characteristics can further be quantitatively analyzed using the Cassie−Baxter equation, given by

$$\cos\theta_c = f\cos\theta - (1 - f)$$

where θ_c and θ are the apparent static water contact angle and the intrinsic water contact angle, respectively. According to this equation, the projected solid area fractions (f) are calculated as 0.64, 0.54, 0.51, and 0.59 for UV/ozone treatment durations of 30, 40, 50, and 60 min, respectively. The estimated projected solid area fraction of macrowrinkle arrays can be expressed as $f = \frac{L_{wetting}}{\lambda}$, in which λ denotes the macrowrinkle wavelength and $L_{wetting}$ represents the projected solid−liquid contact length extending across each macrowrinkle (Figure S16). Using this expression, the corresponding $L_{wetting}$ values are determined to

https://doi.org/10.1021/acsami.6c06369
ACS Appl. Mater. Interfaces 2026, 18, 30329−30339

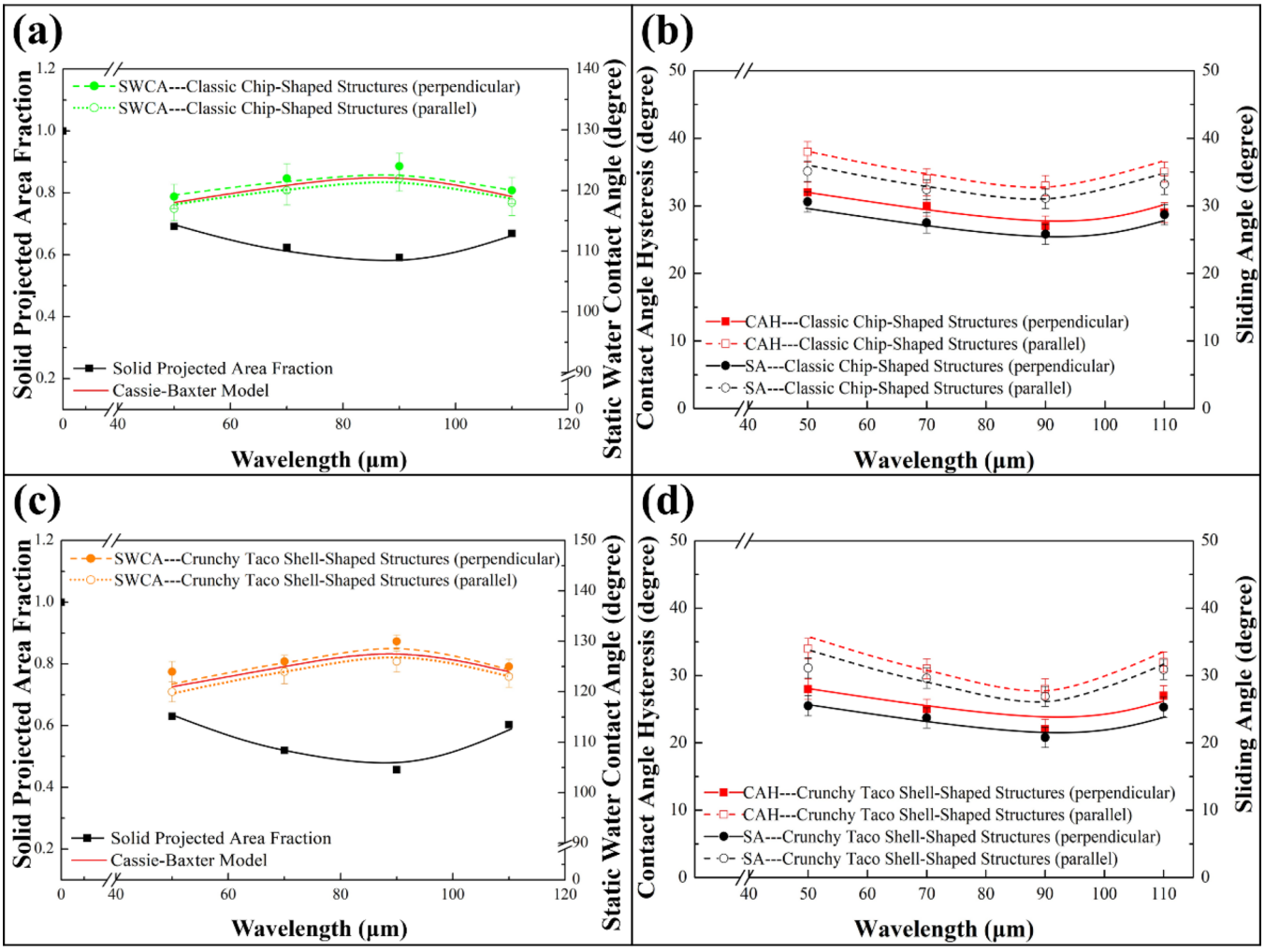

Figure 5. Dependences of (a) the solid projected area fraction (black solid squares), static water contact angle (green circles), (b) water contact angle hysteresis (red squares), and sliding angle (black circles) on the wavelength of the surface-functionalized classic chip-shaped macrowrinkles. Dependences of (c) the solid projected area fraction (black solid squares), static water contact angle (orange circles), (d) water contact angle hysteresis (red squares), and sliding angle (black circles) on the wavelength of the surface-functionalized crunchy taco shell-shaped macrowrinkles. The solid symbols represent the angles measured in the direction perpendicular to the macrowrinkles, while the hollow symbols represent the angles measured in the direction parallel to the macrowrinkles.

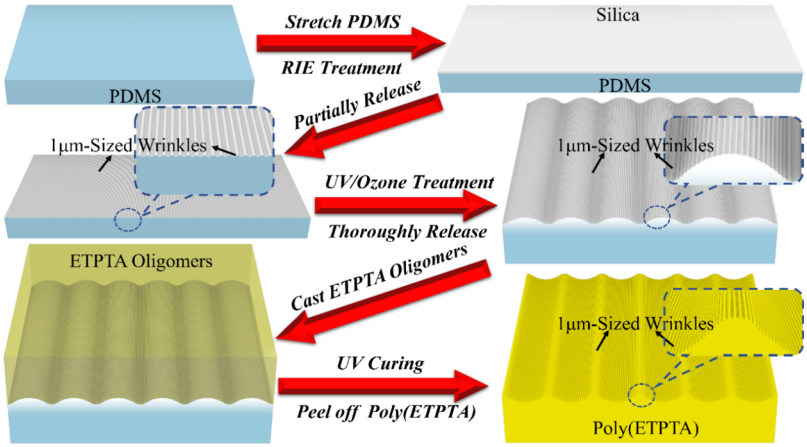

Figure 6. Schematic illustration of the experimental procedures employed to assemble regularly arranged wavy chip-shaped macrowrinkles.

be 32.5, 38.2, 46.8, and 65.9 μm. The findings indicate that roughly half of each classic chip-shaped macrowrinkle becomes wetted upon contact with water, therefore giving rise to low dynamic water contact angles and pronounced water contact angle hysteresis (Figures S17 and S18). As a result, these macrowrinkle arrays exhibit high sliding angles of ~30°, even

https://doi.org/10.1021/acsami.6c06369
ACS Appl. Mater. Interfaces 2026, 18, 30329−30339

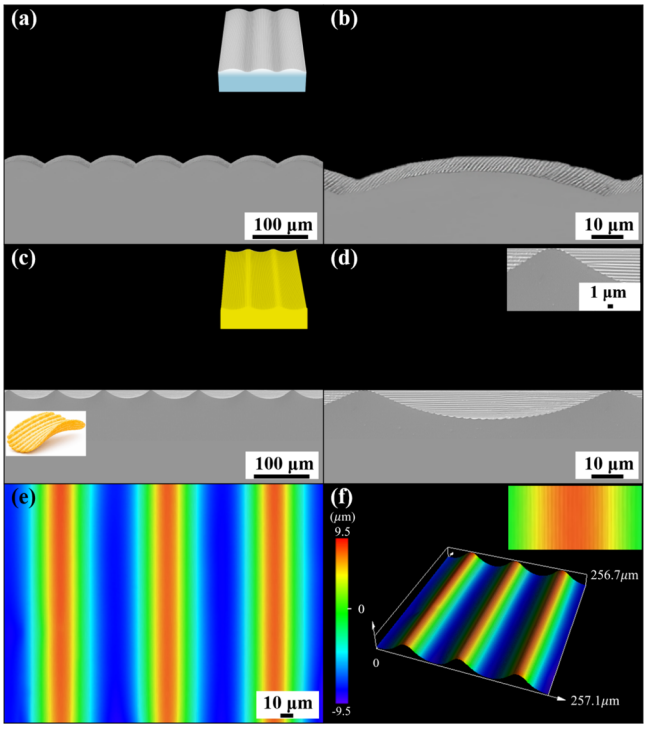

Figure 7. (a) Cross-sectional SEM image of a PDMS mold fabricated by uniaxially stretching a featureless PDMS film to an elongation ratio of 65%, followed by a 2.5 min oxygen plasma and a UV irradiation/ozone treatment for 45 min. (b) Cross-sectional SEM image of a wavy chip-shaped macrowrinkle array-patterned poly(ETPTA) substrate replicated from the PDMS mold. (c) Cross-sectional SEM image, (d) magnified cross-sectional SEM image, (e) top-view LSCM image, and (f) tilted-view LSCM image of the wavy chip-shaped macrowrinkle array-patterned poly(ETPTA) substrate.

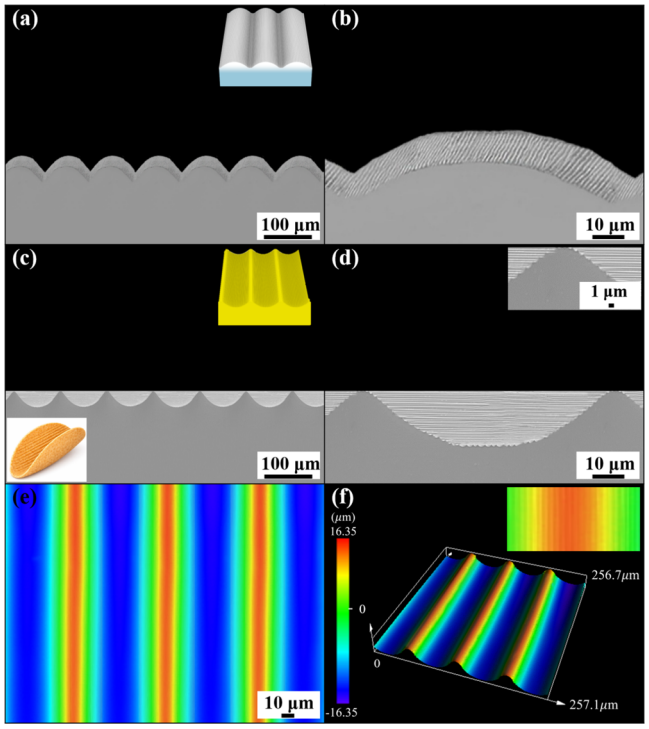

Figure 8. (a) Cross-sectional SEM image of a PDMS mold fabricated by uniaxially stretching a featureless PDMS film to an elongation ratio of 90%, followed by a 2.5 min oxygen plasma and a UV irradiation/ozone treatment for 45 min. (b) Cross-sectional SEM image of a wavy taco shell-shaped macrowrinkle array-patterned poly(ETPTA) substrate replicated from the PDMS mold. (c) Cross-sectional SEM image, (d) magnified cross-sectional SEM image, (e) top-view LSCM image, and (f) tilted-view LSCM image of the wavy taco shell-shaped macrowrinkle array-patterned poly(ETPTA) substrate.

though minor differences in antiwetting behavior are found between the directions parallel and perpendicular to the macrowrinkles.

In addition to the classic chip-shaped macrowrinkle arrays, crunchy taco shell-shaped macrowrinkles with tunable structural geometries are assembled in this study. Rather than an elongation ratio of 25%, PDMS films are uniaxially elongated to a strain of 50%, followed by UV/ozone treatments for varying durations. The application of a higher elongation ratio leads to the development of a larger stiffened surface area, which subsequently generates deeply undulating macrowrinkles upon release of the stretched PDMS film (Figure S19). The as-prepared PDMS stamps can then be used to pattern crunchy taco shell-shaped macrowrinkle arrays. As displayed in Figure 4 and Figures S20–S22, the macrowrinkle amplitudes increase progressively from 8.8, 12.9, 16.3, to 20.8 μm with increasing wavelengths of 49.9, 70.5, 88.9, and 110.1 μm, respectively. Moreover, monotonic increases in both amplitude and wavelength are evident with increasing UV/ozone treatment duration (Figure S23). Compared with classic chip-shaped macrowrinkles, the crunchy taco shell-shaped macrowrinkle arrays markedly reduce the contact area between water and the surface ($\frac{L_{wetting}}{\lambda}$ = 0.53, 0.47, 0.41, and 0.49), resulting in higher static and dynamic water contact angles (Figures S24–S28). Of the macrowrinkle arrays investigated, the one replicated from a PDMS stamp subjected to 50 min of UV/ozone treatment exhibits the highest static water contact angle of 130 ± 1° and the lowest water contact angle hysteresis of 23.8 ± 3°. Importantly, the corresponding sliding angles demonstrate a pronounced directional dependence, with an approximately 6° disparity between measurements parallel and perpendicular to the macrowrinkles. The anisotropic antiwetting characteristics of the macrowrinkle arrays are further analyzed and compared in Figure 5. Despite similar static water contact angles measured in directions parallel and perpendicular to the macrowrinkles, the presence of macrowrinkles facilitates the transport of water droplets along the longitudinal direction of the wrinkled patterns. As a consequence, the sliding angles measured perpendicular to the macrowrinkles are consistently smaller than those measured parallel to the macrowrinkles. Most importantly, this sliding angle difference and the associated anisotropic antiwetting characteristics become more pronounced on deeply undulating macrowrinkles.

These macrowrinkled patterns are further superimposed with microwrinkles (~1 μm in size) by implementing a multistage surface treatment approach to enhance their geometrically driven antiwetting performance (Figure 6). For this approach, uniaxially stretched PDMS films (strain = 65%) are treated with oxygen plasma for 2.5 min and then partially released to an elongation ratio of 25% to induce the formation of microwrinkle arrays. The microwrinkled films are subsequently subjected to UV irradiation/ozone treatment for controlled exposure periods, after which complete strain release is performed to assemble hierarchical wrinkle arrays.

https://doi.org/10.1021/acsami.6c06369
ACS Appl. Mater. Interfaces 2026, 18, 30329–30339

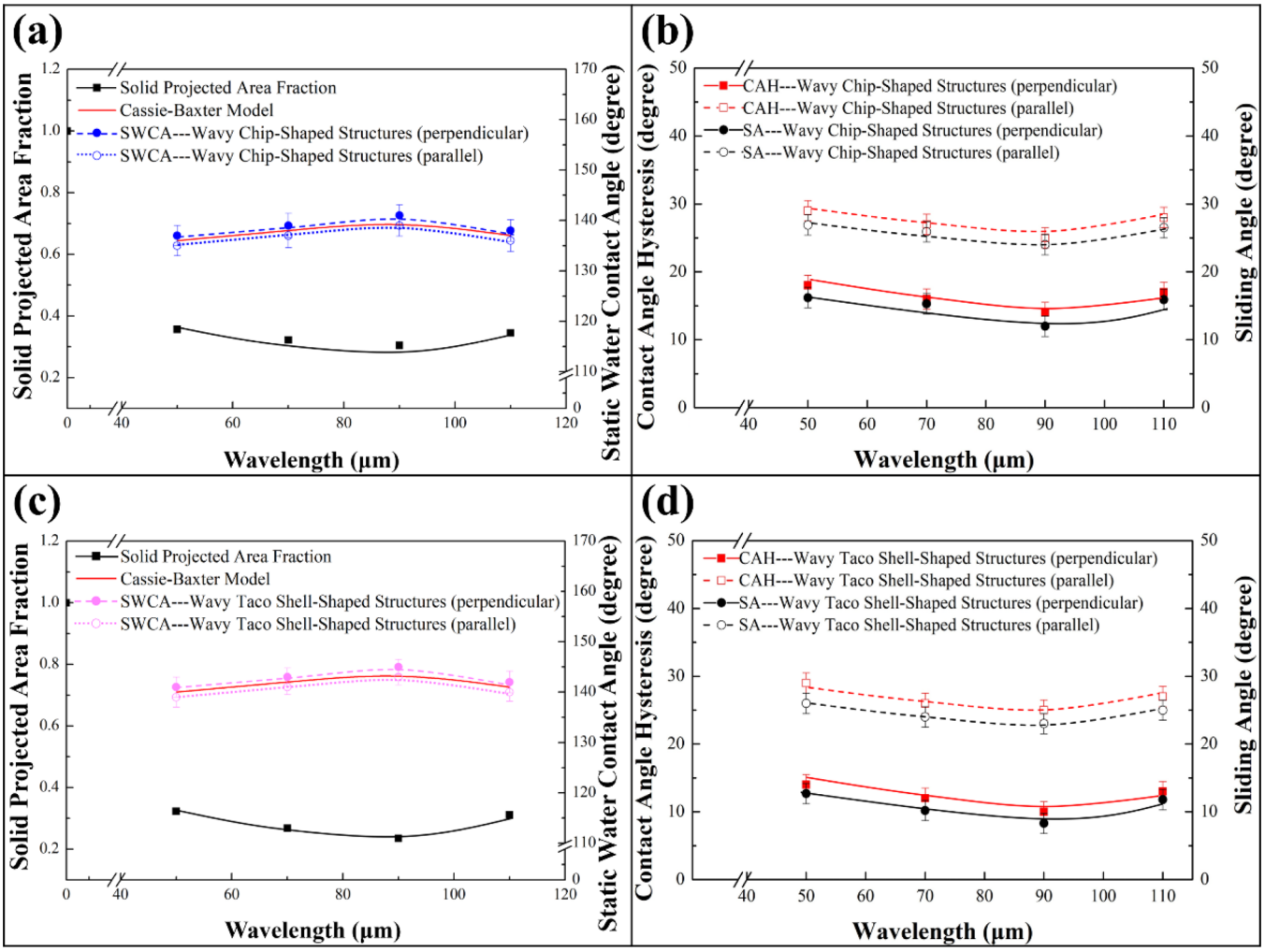

Figure 9. Dependences of (a) the solid projected area fraction (black solid squares), static water contact angle (green circles), (b) water contact angle hysteresis (red squares), and sliding angle (black circles) on the wavelength of the surface-functionalized wavy chip-shaped macrowrinkles. Dependences of (c) the solid projected area fraction (black solid squares), static water contact angle (orange circles), (d) water contact angle hysteresis (red squares), and sliding angle (black circles) on the wavelength of the surface-functionalized wavy taco shell-shaped macrowrinkles. The solid symbols represent the angles measured in the direction perpendicular to the macrowrinkles, while the hollow symbols represent the angles measured in the direction parallel to the macrowrinkles.

Afterward, these structured films are used as replica molds to pattern regularly arranged wavy chip-shaped macrowrinkles (Figure 7 and Figures S29−S31). In place of an initial strain of 65%, uniaxially stretched PDMS films with a strain of 90% are used to pattern wavy taco shell-shaped macrowrinkle arrays, following the aforementioned fabrication procedures (Figure 8 and Figures S32−S35). The wavelengths of the resulting macrowrinkle arrays can be precisely controlled to approximately 50.0, 70.0, 90.0, and 110.0 μm (Figures S36 and S37), which are consistent with those reported for classic chip-shaped and crunchy taco shell-shaped macrowrinkle arrays. Crucially, these macrowrinkles are uniformly overlaid with long-range ordered microwrinkles, and discernible defects are not observed in the SEM and LSCM images.

The presence of microwrinkle arrays significantly reduces the projected solid area fraction (Figures S38 and S39), leading to notable improvements in static and dynamic antiwetting characteristics. For the hierarchical macrowrinkle arrays, the projected solid area fraction (f) can be theoretically estimated using the following expression:

$$f = f_{\text{microwrinkle}} \times \frac{L_{\text{wetting}}}{\lambda}$$

in which $f_{\text{microwrinkle}}$ denotes the projected solid area fraction of the microwrinkle array, L_{wetting} refers to the projected solid−liquid contact length extending across each classic chip-shaped or crunchy taco shell-shaped macrowrinkle, and λ signifies the wavelength of each wavy chip-shaped or wavy taco shell-shaped macrowrinkle. By substituting the previously reported water contact angles of the microwrinkle array into the Cassie−Baxter model, the $f_{\text{microwrinkle}}$ is determined to be 0.72. These calculations yield minimal f values of 0.36 and 0.29 for the wavy chip-shaped and wavy taco shell-shaped macrowrinkle arrays, respectively, with corresponding static water contact angles of 133.2 and 138.2°. As displayed in Figure 9, much higher static water contact angles of 141.0 and 145.1° are achieved on the surface-functionalized wavy chip-shaped and wavy taco shell-shaped macrowrinkle array-patterned substrates, respectively, accompanied by water contact angle hysteresis values of 13.8 and 8.2° measured in the direction perpendicular to the macrowrinkles (Figures S40−S47). It is

https://doi.org/10.1021/acsami.6c06369
ACS Appl. Mater. Interfaces 2026, 18, 30329−30339

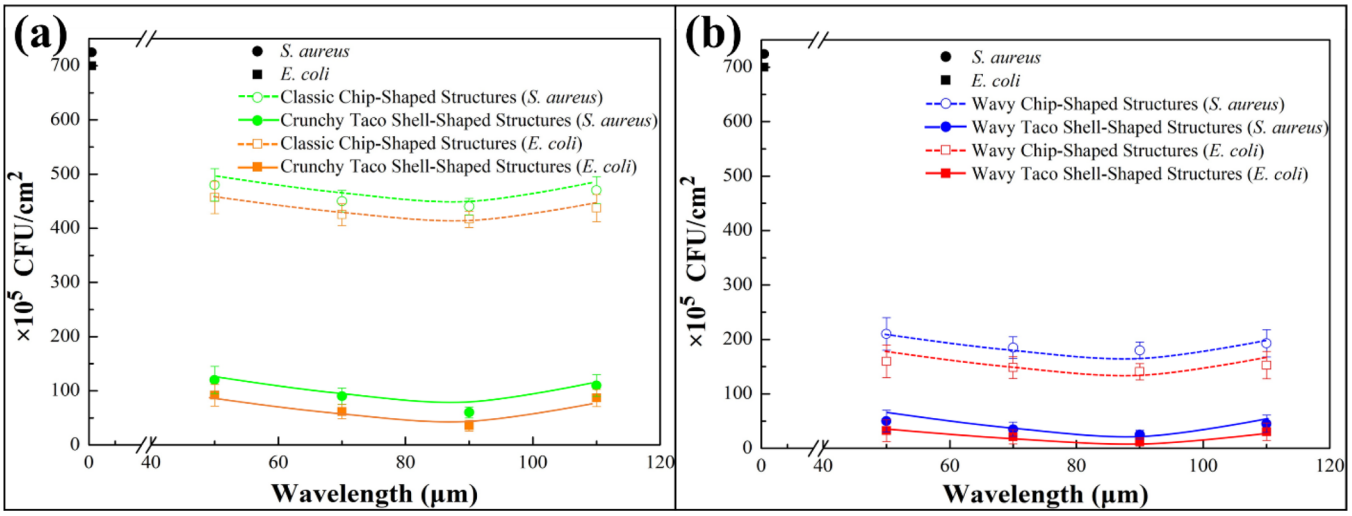

Figure 10. Quantitative analysis of the bacterial colony-forming units (CFU/cm^2) on the surface-functionalized (a) classic chip-shaped macrowrinkle-patterned poly(ETPTA) substrates (hollow symbols), crunchy taco shell-shaped macrowrinkle-patterned poly(ETPTA) substrates (solid symbols), (b) wavy chip-shaped macrowrinkle-patterned poly(ETPTA) substrates (hollow symbols), and wavy taco shell-shaped macrowrinkle-patterned poly(ETPTA) substrates (solid symbols).

believed that the hierarchical geometry further reduces surface energy and stabilizes trapped air layers, thereby enhancing water repellency and enabling low water contact angle hysteresis. By contrast, much larger water contact angle hysteresis values of 25.2 and 23.4° are found in the direction parallel to these macrowrinkles. The anisotropies in water contact angle hysteresis further contribute to an 11.4° disparity in sliding angle between measurements taken parallel and perpendicular to the wavy chip-shaped macrowrinkles, while an even larger disparity of 15.1° is evident on the wavy taco shell-shaped macrowrinkle-patterned substrate. Collectively, these results indicate that the integration of macrowrinkles and microwrinkles is crucial for achieving pronounced anisotropic antiwetting characteristics.

The hierarchically wrinkled structures, therefore, facilitate efficient microbial removal as their surfaces are rinsed with phosphate-buffered saline along the structural features. Compared with the antibacterial performances identified on the classic chip-shaped and crunchy taco shell-shaped macrowrinkle-patterned poly(ETPTA) substrates, the wavy macrowrinkle-patterned substrates demonstrate markedly reduced bacterial colonization, as quantified by colony-forming unit (CFU) analysis (Figure 10). In line with theoretical predictions, the wavy taco shell-shaped macrowrinkle-patterned substrates exhibit the lowest CFU counts for both *S. aureus* (~23.7 × 10^5 CFU/mL) and *E. coli* (~14.6 × 10^5 CFU/mL). Of particular importance, this patterned substrate achieves a bacterial removal efficiency exceeding 96% when benchmarked against the unpatterned substrate (~74.3 × 10^6 CFU/mL). These findings reaffirm that the application of shark scale-inspired wavy surface architectures significantly enhances antifouling efficacy (Figure S48). It is worth noting that the CFU counts of rod-shaped *E. coli* are consistently lower than those of spherical *S. aureus* across all macrowrinkle-patterned substrates. This observed difference arises from the greater susceptibility of rod-shaped bacteria to disruption by surface topography, which enables more effective detachment through geometrically driven anisotropic liquid transports.[43,44] In contrast, the corresponding antifouling capability is substantially suppressed when the rinsing direction is perpendicular to the macrowrinkles (Figures S49 and S50). The results highlight the critical role of structural orientation in the design of antifouling functionality. It is worth mentioning that poly(ETPTA) exhibits high mechanical durability, rendering it suited for long-term applications in aqueous environments.[45] The fluorinated compounds further impart superior chemical stability and low surface energy, enabling the retention of both the surface morphology and corresponding hydrophobicity after prolonged submersion in water for 6 months (Figure S51). Despite these advantages, they inevitably pose potential environmental and health hazards. For environmentally sustainable applications, nonperfluorinated alternatives, such as silicone acrylates, long-chain alkyl acrylates, and biobased monomers, can be seamlessly adopted within the poly(ETPTA) substrate framework.[46]

CONCLUSIONS

Inspired by the antifouling placoid scales located within the caudal peduncle of a shortfin mako shark, well-organized hierarchical wrinkles with tunable structural geometries are self-assembled using a multistage surface treatment approach. It is evidenced that the integration of microwrinkle and macrowrinkle arrays significantly reduces the projected solid−liquid contact area fraction and generates pronounced anisotropic antiwetting behaviors. This unique characteristic results in a 15.1° difference in sliding angle between directions parallel and perpendicular to the wavy taco shell-shaped macrowrinkles, thereby facilitating directional liquid transport and enhancing microorganism removal from the macrowrinkle-patterned substrate. Compared with the antibacterial performance identified on an unpatterned substrate, a bacterial removal efficiency exceeding 96% can be achieved on this patterned substrate. Such hierarchical wrinkle arrays are anticipated to play a crucial role in the development of next-generation antifouling coatings, biomedical devices, microfluidic devices, and liquid transport systems.

https://doi.org/10.1021/acsami.6c06369
ACS Appl. Mater. Interfaces 2026, 18, 30329−30339

■ ASSOCIATED CONTENT

Supporting Information

The Supporting Information is available free of charge at https://pubs.acs.org/doi/10.1021/acsami.6c06369.

Photographic images, SEM images, schemes, and static water contact angles evaluated for shortfin mako sharks in this study (PDF)

■ AUTHOR INFORMATION

Corresponding Authors

Hsiu-Wen Chien − *Department of Chemical and Materials Engineering, National Kaohsiung University of Science and Technology, Kaohsiung 807618, Taiwan;* orcid.org/0000-0001-5596-6281; Email: hsiu-wen.chien@nkust.edu.tw

Hongta Yang − *Department of Chemical Engineering, National Chung Hsing University, Taichung 40227, Taiwan;* orcid.org/0000-0002-5822-1469; Email: hyang@dragon.nchu.edu.tw

Authors

Hsiang-Wen Hsueh − *Department of Chemical Engineering, National Chung Hsing University, Taichung 40227, Taiwan*

Shin-Hua Lin − *Department of Chemical Engineering, National Chung Hsing University, Taichung 40227, Taiwan*

Zi-Xuan Chen − *Department of Chemical Engineering, National Chung Hsing University, Taichung 40227, Taiwan*

Hsin-Yi Yang − *Department of Chemical Engineering, National Chung Hsing University, Taichung 40227, Taiwan*

Yun-Yu Wu − *Department of Chemical Engineering, National Chung Hsing University, Taichung 40227, Taiwan*

Han-Yu Hsueh − *Department of Materials Science & Engineering, National Chung Hsing University, Taichung 40227, Taiwan;* orcid.org/0000-0003-2850-7279

Rong-Ho Lee − *Department of Chemical Engineering, National Chung Hsing University, Taichung 40227, Taiwan;* orcid.org/0000-0002-1373-9360

Complete contact information is available at: https://pubs.acs.org/10.1021/acsami.6c06369

Author Contributions

Hsiang-Wen Hsueh and Shin-Hua Lin contributed equally to this work.

Notes

The authors declare no competing financial interest.

■ ACKNOWLEDGMENTS

The authors acknowledge financial support from the National Science and Technology Council under Grant Nos. NSTC 112-2221-E-005-006-MY3 and 114-2221-E-005-015-MY3.

■ REFERENCES

(1) Hong, H.; Lv, J.; Deng, A.; Tang, Y.; Liu, Z. A Review of Experimental Assessment Processes of Material Resistance to Marine and Freshwater Biofouling. *J. Environ. Manage.* **2024**, *357*, No. 120766.

(2) Qian, P. Y.; Cheng, A.; Wang, R.; Zhang, R. Marine Biofilms: Diversity, Interactions and Biofouling. *Nat. Rev. Microbiol.* **2022**, *20* (11), 671−684.

(3) Satasiya, G.; Kumar, M. A.; Ray, S. Biofouling Dynamics and Antifouling Innovations: Transitioning from Traditional Biocides to Nanotechnological Interventions. *Environ. Res.* **2025**, *269*, No. 120943.

(4) Alnumani, A.; Abutaleb, A.; Park, B.; Mubashir, M. Recent Advancement on Water Filtration Membranes: Navigating Biofouling Challenges. *Environ. Res.* **2024**, *251*, No. 118615.

(5) Hadžić, N.; Jovanović, I.; Vladimir, N. Biofouling of Ships and Offshore Structures: Research Trends and Future Pathways. *Ocean Eng.* **2026**, *347*, No. 123988.

(6) Qiu, Q.; Gu, Y.; Ren, Y.; Ding, H.; Hu, C.; Wu, D.; Mou, J.; Wu, Z.; Dai, D. Research Progress on Eco-Friendly Natural Antifouling Agents and Their Antifouling Mechanisms. *Chem. Eng. J.* **2024**, *495*, No. 153638.

(7) Zhang, X.; Zhang, S.; Mathivanan, K.; Zhang, R.; Zhang, J.; Jiang, Q.; Sand, W.; Duan, J.; Hou, B. Research Progress and Prospects in Antifouling Performance of Photocatalytic Sterilization: A Review. *J. Mater. Sci. Technol.* **2025**, *208*, 189−201.

(8) Rho, H.; Yu, P.; Zhao, Z.; Lee, C. S.; Chon, K.; Perreault, F.; Alvarez, P. J. J.; Amy, G.; Westerhoff, P. Inhibition of Biofouling on Reverse Osmosis Membrane Surfaces by Germicidal Ultraviolet Light Side-Emitting Optical Fibers. *Water Res.* **2022**, *224*, No. 119094.

(9) Luo, H. W.; Lin, M.; Bai, X. X.; Xu, B.; Li, M.; Ding, J. J.; Hong, W. J.; Guo, L. H. Water Quality Criteria Derivation and Tiered Ecological Risk Evaluation of Antifouling Biocides in Marine Environment. *Mar. Pollut. Bull.* **2023**, *187*, No. 114500.

(10) Lee, S. H.; Chen, Y. S.; Chen, C. F.; Albarico, F. P. J. B.; Lim, Y. C.; Wang, M. H.; Chen, C. W.; Dong, C. D. Butyltin Contamination in Fishing Port Sediments After the Ban of Tributyltin Antifouling Paint: A Case of Qianzhen Fishing Port in Taiwan. *Water* **2022**, *14* (5), 813.

(11) Cahill, P. L.; Moodie, L. W.; Hertzer, C.; Pinori, E.; Pavia, H.; Hellio, C.; Brimble, M. A.; Svenson, J. Creating New Antifoulants Using the Tools and Tactics of Medicinal Chemistry. *Acc. Chem. Res.* **2024**, *57* (3), 399−412.

(12) Marzullo, P.; Gruttadauria, M.; D' Anna, F. Quaternary Ammonium Salts-Based Materials: A Review on Environmental Toxicity, Anti-Fouling Mechanisms and Applications in Marine and Water Treatment Industries. *Biomolecules* **2024**, *14* (8), 957.

(13) Jeon, I.; Ryberg, E. C.; Alvarez, P. J.; Kim, J. H. Technology Assessment of Solar Disinfection for Drinking Water Treatment. *Nat. Sustainability* **2022**, *5* (9), 801−808.

(14) Wang, P.; He, B.; Wang, B.; Wang, L.; Yu, H.; Liu, S.; Ye, Q.; Zhou, F. Durable Self-Polishing Antifouling Coating Based on Fluorine-Containing Pyrrolidone Amphiphilic Copolymer-Functionalized Nanosilica. *Prog. Org. Coat.* **2022**, *165*, No. 106706.

(15) Sfameni, S.; Rando, G.; Marchetta, A.; Scolaro, C.; Cappello, S.; Urzì, C.; Visco, A.; Plutino, M. R. Development of Eco-Friendly Hydrophobic and Fouling-Release Coatings for Blue-Growth Environmental Applications: Synthesis, Mechanical Characterization and Biological Activity. *Gels* **2022**, *8* (9), 528.

(16) Wu, X.; Yang, C.; Wu, L.; Zhang, C.; Cui, G.; Xin, Y. Self-Repairing and Anti-Fouling Performance of Anticorrosive Coating in Marine Environment. *Polym. Test.* **2023**, *124*, No. 108090.

(17) Chu, X.; Yang, F.; Tang, H. Recent Advance in Polymer Coatings Combating Bacterial Adhesion and Biofilm Formation. *Chin. J. Chem.* **2022**, *40* (24), 2988−3000.

(18) Muadtrap, M.; Thiramanas, R.; Crespy, D. Amphiphilic Materials for Advanced Antifouling and Anticorrosion Coatings. *Prog. Org. Coat.* **2025**, *207*, No. 109391.

(19) Pan, Z.; Liu, J.; Li, A.; Bai, Y.; Pan, M. Breaking the Antifouling-Adhesion Trade-off in Zwitterionic Hydrogels via Electrostatic Hydration Modulation. *Macromolecules* **2025**, *58* (23), 12666−12677.

(20) Li, S.; Feng, K.; Li, J.; Li, Y.; Li, Z.; Yu, L.; Xu, X. Marine Antifouling Strategies: Emerging Opportunities for Seawater Resource Utilization. *Chem. Eng. J.* **2024**, *486*, No. 149859.

(21) Ciriminna, R.; Bright, F. V.; Pagliaro, M. Ecofriendly Antifouling Marine Coatings. *ACS Sustainable Chem. Eng.* **2015**, *3* (3), 557−565.

(22) Pan, L. C.; Hsieh, S. Y.; Chen, W. C.; Lin, F. T.; Lu, C. H.; Cheng, Y. L.; Chien, H. W.; Yang, H. Self-Assembly of Shark Scale-

Patterned Tunable Superhydrophobic/Antifouling Structures with Visual Color Response. *ACS Appl. Mater. Interfaces* **2023**, *15* (29), 35311−35320.
(23) Lai, C. J.; Chen, Y. J.; Wu, M. X.; Wu, C. C.; Tang, N. T.; Hsu, T. F.; Lin, S. H.; Li, H. F.; Yang, H. Self-Cleaning and Anti-Fogging Hierarchical Structure Arrays Inspired by Termite Wing. *Appl. Surf. Sci.* **2023**, *616*, No. 156484.
(24) Georgakopoulos-Soares, I.; Papazoglou, E. L.; Karmiris-Obratański, P.; Karkalos, N. E.; Markopoulos, A. P. Surface Antibacterial Properties Enhanced Through Engineered Textures and Surface Roughness: A Review. *Colloids Surf. B: Biointerfaces* **2023**, *231*, No. 113584.
(25) Chien, H. W.; Chen, X. Y.; Tsai, W. P.; Lee, M. Inhibition of Biofilm Formation by Rough Shark Skin-Patterned Surfaces. *Colloids Surf. B: Biointerfaces* **2020**, *186*, No. 110738.
(26) Pellegrino, L.; Savorana, G.; Cassina, V.; Campanile, R.; Centola, M.; Belgiovine, C.; Vinci, V.; Klinger, M.; Lecuyer, S.; D'Imprima, E.; Mantegazza, F.; Secchi, E.; Rusconi, R. Reduction of Bacterial Colonization on Buckling-Induced Wrinkled Surfaces under Fluid Shear. *Nat. Commun.* **2026**, *17*, 1234.
(27) Benschop, H. O. G.; Guerin, A. J.; Brinkmann, A.; Dale, M. L.; Finnie, A. A.; Breugem, W. P.; Clare, A. S.; Stübing, D.; Price, C.; Reynolds, K. J. Drag-Reducing Riblets with Fouling-Release Properties: Development and Testing. *Biofouling* **2018**, *34* (5), 532−544.
(28) Hsieh, P. C.; Chien, H. W. Biomimetic Surfaces: Insights on the Role of Surface Topography and Wetting Properties in Bacterial Attachment and Biofilm Formation. *Colloids Surf. B: Biointerfaces* **2023**, *228*, No. 113389.
(29) Bixler, G. D.; Bhushan, B. Rice and Butterfly Wing Effect Inspired Low Drag and Antifouling Surfaces: A Review. *Crit. Rev. Solid State Mater. Sci.* **2015**, *40* (1), 1−37.
(30) Dundar Arisoy, F.; Kolewe, K. W.; Homyak, B.; Kurtz, I. S.; Schiffman, J. D.; Watkins, J. J. Bioinspired Photocatalytic Shark-Skin Surfaces with Antibacterial and Antifouling Activity via Nanoimprint Lithography. *ACS Appl. Mater. Interfaces* **2018**, *10* (23), 20055−20063.
(31) Jung, W. B.; Cho, K. M.; Lee, W. K.; Odom, T. W.; Jung, H. T. Universal Method for Creating Hierarchical Wrinkles on Thin-Film Surfaces. *ACS Appl. Mater. Interfaces* **2018**, *10* (1), 1347−1355.
(32) Schweikart, A.; Fery, A. Controlled Wrinkling as a Novel Method for the Fabrication of Patterned Surfaces. *Mikrochim. Acta* **2009**, *165* (3), 249−263.
(33) Liu, Y.; He, X.; Yuan, C.; Cao, P.; Bai, X. Antifouling Applications and Fabrications of Biomimetic Micro-Structured Surfaces: A Review. *J. Adv. Res.* **2024**, *59*, 201−221.
(34) Ahmad, Z.; Tyagi, G.; Xiang, S.; Heng, J.; Patrício, P.; Teixeira, P. I. C.; Stafford, C. M.; Douglas, J. F.; Cabral, J. T. Surface Wrinkling of Plasma-Exposed PDMS is Caused by Water Vapor Sorption: An Optical Environmental Sensor. *Adv. Funct. Mater.* **2025**, *35* (47), No. 2509167.
(35) Zhang, X. A.; Jiang, Y.; Venkatesh, R. B.; Raney, J. R.; Stebe, K. J.; Yang, S.; Lee, D. Scalable Manufacturing of Bending-Induced Surface Wrinkles. *ACS Appl. Mater. Interfaces* **2020**, *12* (6), 7658−7664.
(36) Wang, Q.; Yu, S.; Ye, Q.; Yang, B.; Zhang, Y.; Wang, X.; Li, L. Controlled Preparation of Highly Stretchable, Crack-Free Wrinkled Surfaces with Tunable Wetting and Optical Properties. *Langmuir* **2024**, *40* (4), 2102−2110.
(37) Li, Y.; Li, J.; Zhang, Q.; Li, K.; Li, Y.; Zhang, C.; Zhang, X.; Li, L.; Tian, D. Electric-Field-Adaptive Wrinkled Surface for Tunable Liquid Manipulation: From Precision Droplet Transport to Selective Screening. *Adv. Funct. Mater.* **2026**, *36* (18), No. e19020.
(38) Vellwock, A. E.; Su, P.; Zhang, Z.; Feng, D.; Yao, H. Reconciling the Conflict between Optical Transparency and Fouling Resistance with a Nanowrinkled Surface Inspired by Zebrafish's Cornea. *ACS Appl. Mater. Interfaces* **2022**, *14* (6), 7617−7625.
(39) Cai, Z. X.; Chen, F. Z.; Tian, Y. L.; Zhang, D. W.; Lian, Z. X.; Cao, M. Y. Programmable Droplet Transport on Multi-Bioinspired Slippery Surface with Tridirectionally Anisotropic Wettability. *J. Chem. Eng.* **2022**, *449*, No. 137831.
(40) Sun, Q.; Yang, Z.; Wang, Z.; Wu, L. Anti-fouling Performance Investigation of Micron-Submicron Hierarchical Structure PVDF Membranes in Water-in-Oil Emulsion Separation. *J. Environ. Chem. Eng.* **2022**, *10* (3), No. 107497.
(41) Matsuyama, K.; Tanaka, S.; Okuyama, T. Hydrophobic Modification of Fibers by Pressure-Induced Phase-Separation Coupled with Ultrasonic Irradiation in High-Pressure Liquid Carbon Dioxide. *Chem. Eng. J.* **2014**, *246*, 106−113.
(42) Liu, N.; Sun, Q.; Yang, Z.; Shan, L.; Wang, Z.; Li, H. Wrinkled Interfaces: Taking Advantage of Anisotropic Wrinkling to Periodically Pattern Polymer Surfaces. *Adv. Sci.* **2023**, *10* (12), No. 2207210.
(43) Oguntade, E.; Owuor, L.; Du, C.; Acierto, A.; Meyer, S.; Monroe, M. B. B.; Henderson, J. H. Bacterial Response to Shape-Memory Actuated Silk Wrinkled Surface Topographies as a Strategy for Biofilm Prevention. *Adv. Mater. Interfaces* **2025**, *12* (6), No. 2400684.
(44) Li, C.; Li, F.; Wang, K.; Zhao, Y.; Xie, D. Antimicrobial Packaging Film with Finger Wrinkles Structures Based on Egg White and Chitosan Coating for Fruit Preservation. *Int. J. Biol. Macromol.* **2024**, *283*, No. 137888.
(45) Chen, Y. J.; Fang, C. Y.; Huang, Y. W.; Hsu, T. F.; Tang, N. T.; Tsai, H. P.; Lee, R. H.; Lin, S. H.; Hsuen, H. W.; Lin, K. Y. A.; Yang, H. White Roman Goose Feather-Inspired Unidirectionally Inclined Conical Structure Arrays for Switchable Anisotropic Self-Cleaning. *ACS Appl. Mater. Interfaces* **2024**, *16* (28), 36840−36850.
(46) Li, W.; Chang, Y.; Tian, J.; Min, J.; Ding, F. Methyl-Enriched Siloxane-co-Acrylate Fluorine-Free Finishing Agent Enables Durable Antisoiling on Polyester Fabrics. *Langmuir* **2026**, *42* (9), 6814−6824.

https://doi.org/10.1021/acsami.6c06369
ACS Appl. Mater. Interfaces 2026, 18, 30329−30339